Efficiency of core-level interatomic Coulombic decay in rare-gas dimers

Liping Liu [1,2] Přemysl Kolorenč,[3] and Kirill Gokhberg [2]

[1]*Department of Physics, National University of Defense Technology, Changsha, Hunan 410073, People's Republic of China*
[2]*Theoretische Chemie, Physikalisch-Chemisches Institut, Universität Heidelberg, Im Neuenheimer Feld 229, D-69120 Heidelberg, Germany*
[3]*Charles University, Faculty of Mathematics and Physics, Institute of Theoretical Physics, V Holešovičkách 2, 18000 Prague, Czech Republic*

(Received 20 September 2019; accepted 4 February 2020; published 4 March 2020)

In this work we investigated the competition between the local Auger decay and core-level interatomic Coulombic decay (ICD) processes in core ionized rare-gas dimers. We computed the respective partial decay widths for the $4d$ vacancy in Xe_2, XeKr, and XeAr, as well as for the $3d$ vacancy in Kr_2. We found that the efficiency of ICD is strongly increased with decreasing interatomic distance and decreasing energy transfer in the decay step. The ICD-to-Auger ratio in the Franck-Condon region, where the decay occurs, is at most 0.26%. However, it reaches a few percentage points in larger clusters and becomes amenable for experimental observation. The small value of the branching ratio is due to large interatomic distances in the dimers (4–4.4 Å). Our results also indicate, in accordance with previous measurements, that in hydrogen-bonded and microsolvated clusters, where the distances between the monomers are 2–3 Å, core-level ICD should become an important pathway for charge redistribution following the absorption of hard x-rays.

DOI: 10.1103/PhysRevA.101.033402

I. INTRODUCTION

Studying the response of small organic molecules which contain a covalently bound high-Z atom to the action of hard-x-ray radiation is the first step in understanding the avalanche of processes initiated by x-rays in biomolecular samples [1]. Hard x-rays are predominantly absorbed by the heavy atom so that a deeply lying electronic core vacancy is formed. A short time later the molecule becomes multiply ionized and is destroyed in a Coulomb explosion. While the ultimate fate of the molecule is clear, the pathways by which the energy and charge are redistributed throughout and the characteristic rates of electron and nuclear dynamics are much less so. The details of energy and charge redistribution has been sought in a number of experiments which involve iodinated organic molecules interacting with a short XFEL pulse of up to few tens of femtosecond duration [2–6]. Thus, it was found that, within 10 fs following the creation of a vacancy in the L-shell of iodine in five-iodouracil [4], the total molecular charge can be as large as 14. By this time the molecule loses all its hydrogen atoms, while the C–C, C–N, and C–O bonds grow by a few percentage points and become fully dissociated after 30 fs. This spectacular rate of charge accumulation and redistribution is attributed to the absorption of multiple photons in the XFEL pulse, and to the ultrafast nature of the Auger decay cascades initiated by the creation of the L vacancy in the iodine. In particular, while the initial stages of the cascade involve tightly bound iodine electrons and lead to the accumulation of positive charge on the I atom, the later stages involve electrons from the delocalized molecular orbitals of the organic fragment. Therefore, the accumulation of positive charge and its spreading over the molecule proceed simultaneously as part of a fast Auger decay cascade.

This prompt charge redistribution initiates nuclear dynamics which result in the destruction of the molecule within a short time of only a few tens of femtoseconds. However, biomolecules are normally surrounded by a solvating layer of water molecules. It was proposed that such a solvating layer might hinder the breakup of the irradiated molecule by taking up some of the generated positive charge [7,8]. The charge redistribution mechanism between the molecule and protective layer will certainly depend on the molecular sample and the frequency and intensity of the laser. Thus, it was argued that, in XeAr clusters, which can serve as a suitable model for more complex solvated systems, irradiated by intense extreme-ultraviolet (XUV) light it occurs as the result of electron dynamics and spatially nonuniform electron-ion recombination in a nanoplasma [9,10]. Alternatively, charge-transfer processes between the multiply ionized sample and the atoms or molecules in the solvating layer might also drive the charge redistribution. These processes include electron transfer [2] and electron-transfer-mediated decay (ETMD) [11–13]—all of which start following the termination of the Auger decay cascade.

Electron transfer over the distance of a few angstroms characteristic for the solvated systems takes a short time of only a few tens of femtoseconds [11]. Although fast, it is still slower than the charge redistribution in covalently bound molecules which proceeds within a few femtoseconds, apace with the Auger decay. However, a little consideration shows that, in weakly bound systems, the Auger decay runs concurrently with a process whereby the relaxation of a core vacancy on one atom or molecule leads to the emission of an electron from a neighbor. Such a process was originally put forward to explain the broadening of core photoemission lines in the x-ray photoelectron spectra of metal oxides and halides [14,15]. It is an energy-transfer process between an electronically excited atom or molecule and its weakly bound neighbor, which results in the ionization of the latter, and as such it is related to interatomic Coulombic decay (ICD)

[16]. Originally, the ICD process was formulated for the systems where Auger decay or local autoionization were energetically forbidden. However, later research showed that local autoionizing states may also decay via energy transfer to and ionization of the neighbor, and indeed that this process can dominate the local decay [17–22]. Due to the close mechanistic relation to ICD, it is usual to refer to such decay pathways of autoionizing states as ICD. For the relaxation of a core vacancy, such process is usually called core-level ICD [22]. Importantly, in a solvated molecule this process would produce the positive charge directly in the solvation shell and prevent its accumulation on the molecule.

Both core-level ICD and the Auger decay contribute to the relaxation of core vacancies in a weakly bound chemical environment. The total decay rate of a core vacancy is, therefore, larger than the Auger rate of the corresponding states in the gas phase. This implies that, if it takes place, charge redistribution via ICD following the absorption of an x-ray photon is very fast. Its efficiency, however, depends on the magnitude of the ICD-to-Auger branching ratio. Earlier works in ionic solids argued that this ratio is low and the broadening of photoemission peaks can be explained by the coupling to phonons [23,24]. Later accurate calculations of Auger spectra in XeF_n, which arise from the decay of a $4d$ vacancy in Xe, showed that ICD becomes dominant for the number of neighbors $n > 4$ [25]. The presence of core-level ICD in water clusters and liquid water was suggested by the appearance of a high-energy shoulder on the O($1s$) peak in the Auger-electron spectra, which indicated that two-hole states delocalized over two water molecules were populated [26]. Careful theoretical analysis of the spectra found that the ICD-to-Auger ratio in liquid water can be as high as $2:3$ [27,28]. A clear experimental signature of core-level ICD was observed following core ionization of metal cations in KCl and $CaCl_2$ solutions [21,22]. The experimentally determined ICD-to-Auger branching ratios for K^+ and Ca^{2+} were 1.9% and 9.5%.

The efficiency of ICD depends strongly on three parameters: the amount of energy transferred from the excited species to its neighbor (virtual photon energy [29]), the distance between the participating monomers, and the number of ionizable nearest neighbors [30,31]. Indeed, the increase in the efficiency of the core-level ICD in the series of hydrated K^+ and Ca^{2+} cations was attributed to the shortening of the respective ion-oxygen distances [22]. However, the effect of shorter interatomic distances might be offset by the increase in the virtual photon energy. Thus, the ion-oxygen distance in $Mg^{2+}(H_2O)_6$ is 0.4 Å shorter than in $Ca^{2+}(H_2O)_6$ [32]. However, the theoretical ICD to *KLL*-Auger branching ratio in $Mg^{2+}(H_2O)_6$ is only 3% [11] as compared with 9.5% found for $Ca_{aq}{}^{2+}$. The discrepancy can be explained by the fact that core-level ICD in $Mg_{aq}{}^{2+}$ involves virtual photon energy ($\approx$1200 eV) which is three times larger than in $Ca_{aq}{}^{2+}$.

Since the rare-gas clusters are composed of weakly interacting atoms, they are particularly suitable systems for elucidating the details of electronic processes in condensed media [33,34]. Of particular importance for the study of the core-level ICD process is the recent development of a new electron-photon coincidence technique which allows us to isolate weak core-level ICD signals in electron spectra of such clusters [35]. Indeed, recent application of this technique allowed accurate determination of core ICD signal in Ar clusters [36]. The availability of suitable experimental methods together with theoretical calculations should lead to a better understanding of this important charge-redistribution process. To investigate in detail the effect of virtual photon energy and interatomic distances on the efficiency of the core-level ICD we computed *ab initio* and present below the Auger and ICD rates of $Xe^+(4d^{-1})$ state in Xe_2, XeKr, and XeAr dimers, as well as the respective rates for the $3d$ vacancy in Kr_2.

II. COMPUTATIONAL METHODS

To compute the electronic decay width of an unstable electronically excited state one needs, in addition to computing the decaying state itself, to know which final states are energetically allowed and which are forbidden. Since $Xe^+(4d^{-1})$-R (R = Xe, Kr, Ar) vacancy decays both in the Auger and ICD processes, the decay channels can be both of RXe^{2+} and of R^+Xe^+ character. To find the decaying states and the open and closed one-site and two-site channels, we computed the respective single-ionization energies of the $Xe^+(4d^{-1})$-R states together with the double-ionization energies at different interatomic distances. The results are presented as the potential-energy curves (PECs) of the corresponding states, which are obtained by adding a ground-state PEC to the ionization energies. All computed PECs were adjusted so that the values at infinite separation correspond to the experimental NIST values [37] or to the experimental binding energy of the $Xe^+(4d^{-1})$ state. Since the PECs were computed by nonrelativistic methods, we used the weighted averages over the spin-orbit split multiplets to determine the energies of the atomic terms.

The single- and double-ionization energies were computed within the framework of the nonrelativistic algebraic diagrammatic construction (ADC) method as formulated for the Green's functions [38] and for the two-particle propagator [39]. The extended second-order ADC(2)x scheme [40] was used for the single-ionization potential, while the strict second-order ADC(2) scheme was used for the double-ionization potential. The aug-cc-pwCV5Z basis set was used on argon [41], and the cc-pwCV5Z-PP basis set on xenon [42] and krypton [42] atoms. A 28 electron effective core potential (ECP) [43] and a 10 electron ECP [43] were used for xenon and krypton atoms, respectively, in order to take the scalar relativistic effects into account. The Hamiltonian matrices were diagonalized by using the iterative block-Lanczos procedure [44] which allows fast convergence to the ionization main states.

As discussed below, the decay of the core vacancies occurs in the Franck-Condon region around the equilibrium geometries of the electronic ground states. The equilibrium geometry corresponds to the minimum of the respective PEC, while the Franck-Condon region can be defined as the width of the ground-state vibrational distribution. The PEC of the Xe_2 ground state was computed by using the semiempirical HFD-B formula [45] which combines the multipole expansion for the long-range behavior of the potential curve with the exponential repulsive wall. The empirical parameters were taken from Ref. [46]. The XeAr and XeKr ground-state PECs were computed by using the coupled cluster singles, doubles,

and perturbative triples [CCSD(T)] method using the MOLPRO package [47]. The same basis sets and effective core potentials as in the calculation of ionization energies were used. To obtain the ground-state vibrational wave function in the PEC of interest we used the relaxation method [48].

The partial ICD and Auger decay widths as well as the total decay width of the $Xe^+(4d^{-1})$-R states were computed by using the Fano-ADC-Stieltjes method [49]. This method relies on the Fano-Feshbach theory [50,51], according to which a resonance state is composed of a bound $|\Phi\rangle$ and continuum $|\chi_{\beta,\epsilon_\beta}\rangle$ components, where the continuum component describes the motion of the free electron of energy ϵ_β in the open channel β. The partial decay width into a specific channel is given by

$$\Gamma_\beta = 2\pi |\langle \Phi | \hat{H} - E_r | \chi_{\beta,\epsilon_\beta} \rangle|^2, \tag{1}$$

where $E_r \approx \langle \Phi | \hat{H} | \Phi \rangle$ is the real part of the resonance energy. The total width is obtained from Eq. (1) by summing over all open channels.

To construct the bound-like and continuum components of the resonance wave function we used the ADC(2)x method for the Green's function. The intermediate-state representation formulation of ADC [52] allows us to separate the electronic configuration space of the problem into the decaying state subspace Q and the subspaces P_β corresponding to the final states of different processes. To this end, we employ the generalized localization procedure as described in Refs. [12,53]. To determine P_β, the two-hole-one-particle (2h1p) sub-blocks of the ADC(2)x Hamiltonian, defined by the particle orbital p, are successively diagonalized. Resulting symmetrized 2h1p configurations approximately describe scattering states which correspond either to open or closed two-hole decay channels. By comparing the obtained eigenvalues to the accurate energies of the final states, the symmetrized 2h1p configurations can be assigned to individual channels β and used to construct the projectors P_β. The subspace of the closed channels is then defined as $Q = 1 - \sum_\beta P_\beta$. The diagonalization of the projected electronic Hamiltonians H_{QQ} and $H_{P_\beta P_\beta}$ provide $|\Phi\rangle$ and $|\chi_{\beta,\epsilon_\beta}\rangle$. Since square-integrable Gaussian-type functions were used as the basis set in the calculations, we employed the Stieltjes imaging technique [54–56] for proper normalization of the continuum component.

Restricted Hartree-Fock reference state and the two-electron matrix elements necessary for the width calculations were obtained using MOLCAS quantum chemistry package [57]. The cc-pwCV5Z-PP basis set was utilized on xenon and krypton, while the aug-cc-pwCV5Z basis set was used on argon. To better describe the pseudocontinuum of electronic states the basis sets on Ar, Kr, and Xe were augmented by 5 s-type, 5 p-type, 5 d-type, and 5 f-type Kaufmann-Baumeister-Jungen continuum-like functions [58] (see Supplementary Material [59]). High energies of Auger and core-level ICD electrons require large numbers of additional functions in the basis sets to better describe faster oscillations of the scattering wave functions. The scalar relativistic effects were taken into account by including ECP in the basis sets of xenon and krypton.

To understand the effect of larger virtual photon energy on the efficiency of core-level ICD we computed the partial decay widths of the $3d$ vacancies in Kr_2. The same ADC schemes as for the XeRG dimers were used to compute the decaying and final states. The PEC of the Kr_2 ground state was also computed by using the semiempirical HFD-B formula [45] with the empirical parameters taken from Ref. [46]. The same basis set as given above was used on Kr in the calculation of the PECs and decay widths.

III. RESULTS AND DISCUSSION

The potential-energy curves of the Xe_2, $Xe^+(4d^{-1})Xe$ and Xe_2^{2+} states are shown in Fig. 1. The uppermost panel of Fig. 1 shows the PECs of the decaying states $Xe^+(4d^{-1})Xe$. There are 10 molecular terms—$^2\Sigma_{g,u}$, $^2\Pi_{g,u}$, and $^2\Delta_{g,u}$—of the dimer correlating with the $Xe^+(4d^{-1}\ ^2D) + Xe$ atomic states at infinite interatomic distance $\mathcal{R}$. These states are degenerate as $\mathcal{R} \to \infty$ and lie at 68.34 eV [60] relative to the ground state of Xe_2. They are weakly bound with binding energies lying between 120 and 170 meV. Their minima lie around 3.9 Å, i.e., at shorter distances as compared with the ground-state equilibrium distance $\mathcal{R}_{eq} = 4.4$ Å of Xe_2.

All doubly ionized Xe_2^{2+} states with energies lower than the energy of the $Xe^+(4d^{-1})Xe$ states are possible final states of the electronic decay. In the present work we only consider main (2h-like) doubly ionized states. Decay into the shake-up (3h1p-like) satellite states cannot be described within the ADC(2)x scheme, since it does not explicitly include the necessary 3h2p configurations. There are 64 2h-like open channels which appear as nine energetically distinguishable groups, as shown in the middle panel of Fig. 1. They can be divided into two classes: one-site states of $Xe^{2+}Xe$ character and two-site Xe^+Xe^+ states. At asymptotically large interatomic distances the electron orbitals of the dimer are the atomic orbitals of the isolated Xe atom. Therefore, at such distances the two types of final states represent ideal localized and delocalized dicationic states. Since the Auger decay occurs locally on the atom which bears the initial core vacancy, it populates the one-site final states. Another process which produces the one-site states in Xe_2 is electron-transfer-mediated decay (ETMD) [61]. However, as computations show, its rate for deeply lying vacancies in van der Waals dimers is negligible compared with the Auger rate [62]. The theoretical results are further confirmed by the fact that to date ETMD was observed experimentally only for the states for which the ICD channel is either closed or very slow [63–65]. Therefore, the partial width computed by using the one-site final states is due to the Auger decay. The PECs of the final Auger states are bound. However, since the resulting electronic states are excited, they decay over time into the repulsive $Xe^{2+}Xe^+$ or Xe^+Xe^+ states. The $Xe^{2+}(5s^{-2})Xe$ state undergoes collective ICD [66] into the $Xe^{2+}Xe^+$ manifold, while $Xe^{2+}(5p^{-2})Xe$ and $Xe^{2+}(5p^{-1}5s^{-1})Xe$ will undergo radiative charge transfer [67,68] into the Xe^+Xe^+ states.

The latter two-site states can be also reached directly in the core-level ICD process. The leading ICD channel is $Xe^+(5p^{-1})Xe^+(5p^{-1})$, which at $\mathcal{R}_{eq}$ lies approximately 5 eV below the dominant Auger $Xe^{2+}(5p^{-2})Xe$ channel. As the result, the signatures of the two processes are distinguishable in electron spectra where an ICD peak would appear at the high-energy side of the dominant Auger peak. The weaker ICD peaks due to the decay in the $Xe^+(5p^{-1})Xe^+(5s^{-1})$ and

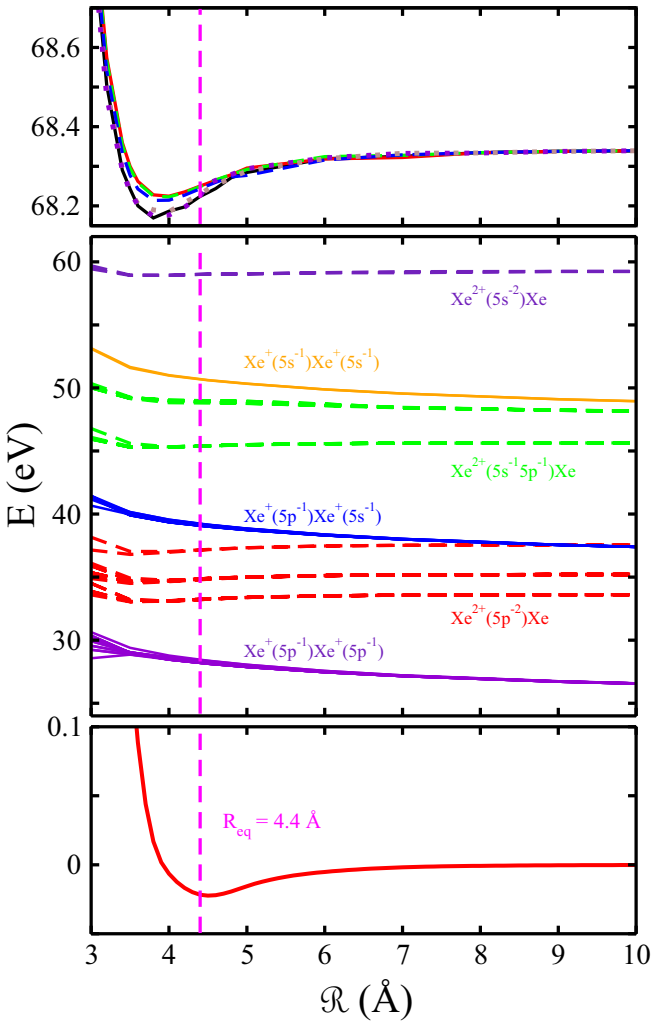

FIG. 1. Potential-energy curves (PECs) of the Xe_2, $Xe^+(4d^{-1})Xe$ and $(Xe_2)^{2+}$ states. (bottom) The ground state of the xenon dimer. (top) The PECs of the decaying singly ionized $Xe^+(4d^{-1})Xe$ states: $^2\Sigma_g$ (black solid line), $^2\Sigma_u$ (red solid line), $^2\Delta_g$ (green dashed line), $^2\Delta_u$ (blue dashed line), $^2\Pi_g$ (brown dotted line), $^2\Pi_u$ (violet dotted line). The PEC of the $^2\Sigma_u$ term lies above the PEC of the $^2\Sigma_g$ term. The PECs of the gerade and ungerade terms of the Π and Δ symmetry are very close and can be barely distinguished. (middle panel) $(Xe_2)^{2+}$ final states which appear as six distinct groups, of which three comprise the two-site ICD final states (solid lines) and three the one-site Auger final states (dashed lines). The ICD states in order of increasing energy correspond respectively to the configurations $Xe^+(5p^{-1})Xe^+(5p^{-1})$, $Xe^+(5p^{-1})Xe^+(5s^{-1})$, and $Xe^+(5s^{-1})Xe^+(5s^{-1})$. The Auger states in order of increasing energy correspond respectively to the configurations $Xe^{2+}(5p^{-2})Xe$, $Xe^{2+}(5p^{-1}5s^{-1})Xe$, and $Xe^{2+}(5s^{-2})Xe$. The ground-state equilibrium distance $\mathcal{R}_{eq} = 4.4$ Å of neutral Xe_2 is shown as a vertical dashed line.

$Xe^+(5s^{-1})Xe^+(5s^{-1})$ states overlap with the Auger-electron spectra, but can still be distinguished at sufficient experimental resolution.

When the two Xe atoms are brought closer to each other, the valence orbitals of the two atoms start to overlap. This orbital overlap is not significant for the interatomic distances considered in this paper. However, the emerging molecular

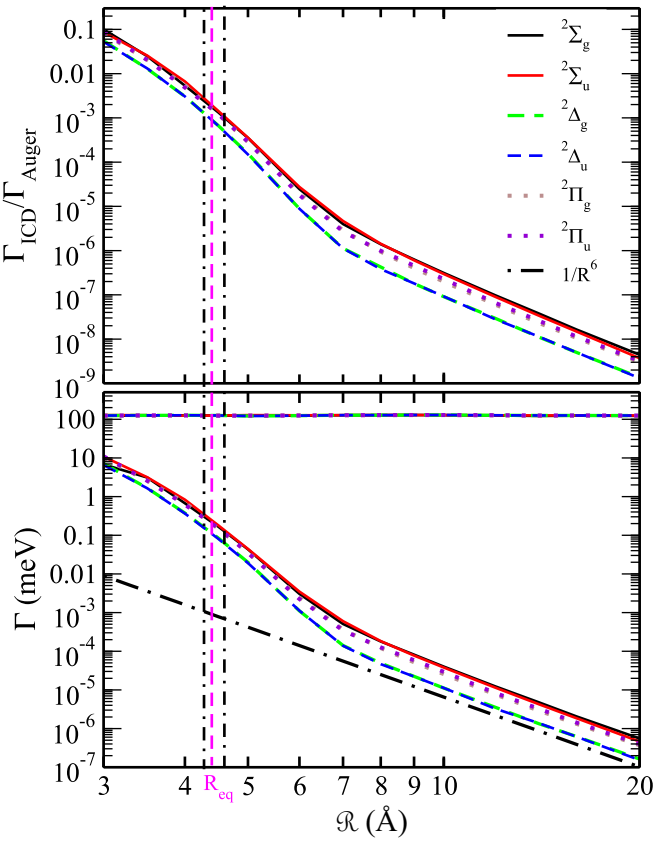

FIG. 2. (bottom) Auger (horizontal lines at 125 meV) and ICD partial decay widths of the decaying singly ionized $Xe^+(4d^{-1})Xe$ states. The Auger widths lie within a 6 meV band and appear as one line in the plot. The ICD widths of the $Xe^+(4d^{-1})Xe$ states—$^2\Sigma_g$ (black solid line), $^2\Sigma_u$ (red solid line), $^2\Delta_g$ (green dashed line), $^2\Delta_u$ (blue dashed line), $^2\Pi_g$ (brown dotted line), $^2\Pi_u$ (violet dotted line)—show the characteristic $\mathcal{R}^{-6}$ behavior of the energy-transfer processes at large distances, while they deviate from it due to the effect of orbital overlap starting at 7 Å. The widths of the gerade and ungerade terms of the same linear symmetry are very close and can be barely distinguished. The plot of the $\mathcal{R}^{-6}$ function (dashed-dotted line) is included to accentuate the behavior of ICD widths at large $\mathcal{R}$. (top) ICD-to-Auger branching ratios. The ground-state equilibrium distance, $\mathcal{R}_{eq}$, of the neutral Xe_2 is shown as a vertical dashed line. The Franck-Condon region is marked by the dashed-dotted vertical lines.

orbitals are not strictly localized on a specific atom, so that the one-site final states acquire some nonlocal and the two-site states some local character. The most visible effect of the orbital overlap and the resulting one-site and two-site channels mixing is the enhancement of the ICD width relative to the asymptotic energy-transfer value, as we discuss in detail below. This mixing also occurs at larger interatomic separations whenever a one-site state and a two-site state cross, as illustrated by the crossing of the $Xe^+(5p^{-1})Xe^+(5s^{-1})$ and $Xe^{2+}(5p^{-2})Xe$ PECs at 9 Å. However, in the Xe dimer, due to a very short lifetime of the core-hole, the decay occurs in the Franck-Condon region around $\mathcal{R}_{eq}$ where the ICD and Auger channels are clearly separated.

The partial Auger and core-level ICD decay widths are shown in the lower panel of Fig. 2. The Auger widths lie

within a narrow band of 6 meV varying randomly about the average asymptotic value due to the numerical errors of the Stieltjes-Fano technique. The average asymptotic value found in our computation was 125 meV. To estimate the accuracy of our nonrelativistic result we note that the relativistic corrections lead to the splitting of the $4d^{-1}$ atomic state into the $4d_{5/2}$ and $4d_{3/2}$ states. To the lowest order the nonrelativistic width is the weighted average of the widths of the relativistic states [69]. The experimental Auger widths of the $4d_{5/2}$ and $4d_{3/2}$ states of the Xe atom were previously found to be 105—115 meV and 112—130 meV, respectively [70]. Full relativistic calculations for the corresponding states at the Dirac-Fock and ADC(2)x levels produced 160 meV (143 meV) [71], and 162 meV (132 meV) [72], respectively, for the $4d_{5/2}$ ($4d_{3/2}$) states. The value of our nonrelativistic calculation lies between the experimental values for the two $4d$ multiplets, which shows that it accurately represents the decay in Xe. Within the numerical error the computed Auger widths of all molecular $Xe^+(4d^{-1})Xe$ terms stay constant with the interatomic distance $\mathcal{R}$. Also, the Auger widths are the same for the terms of different symmetry. This indicates that Auger decay in the weakly bound Xe dimer remains essentially a local atomic process.

In contrast to the behavior of the Auger widths, the core-level ICD widths vary strongly with the interatomic distance. They behave as $1/\mathcal{R}^6$ from the asymptotic distances up to 7 Å reflecting the dipole-dipole nature of ICD at large interatomic distances [30,73]. At shorter distances the widths grow faster than $1/\mathcal{R}^6$ due to the effect of orbital overlap [30]. Moreover, the ICD widths of different molecular terms are different, even at asymptotic distances. This is due to the fact that the coupling of two Σ transition dipoles leads to energy transfer which is four times more efficient than that due to the coupling of two Π transition dipoles [31,74]. The ratios between the ICD widths corresponding to different terms lie below four due to the fact that transitions proceed from a given decaying state into several final states, so that there are no cases of pure Σ-Σ or Π-Π couplings. However, the $\Gamma^{\rm ICD}_{\Sigma}/\Gamma^{\rm ICD}_{\Pi}$ ratio reaches 3.3 and comes close to the highest possible value of four.

The ICD widths at $\mathcal{R}_{\rm eq}$ lie between 0.1 and 0.25 meV and are more than two orders of magnitude smaller than the Auger decay rates. The shortest distance at which two bound Xe atoms can be found in the decaying state is $\mathcal{R} = 3.4$ Å. It approximately corresponds to the position of the inner classical turning point in the decaying-state PECs which is obtained at the dissociation energy of the respective PECs. The ICD widths at the inner turning point lie between 2 and 4 meV. Therefore, the largest ICD-to-Auger branching ratio in Xe_2 shown in the upper panel of Fig. 2 varies between 0.2% and 3.2% for the interatomic distances at which the electronic decay is possible in a bound Xe dimer. Due to the very short overall lifetime of the core-hole state no nuclear motion will take place in the decaying state and the decay will occur in the Franck-Condon region. Therefore, the value of 0.2% is the one which will be observed in a Xe dimer. In larger clusters the ICD width would grow linearly with the number of nearest neighbors of the $Xe^+(4d^{-1})$ ion. If we assume that the Xe cluster has the face-centered cubic lattice, a bulk atom would have 12 neighbors. Therefore, in large clusters the ICD-to-Auger ratio can reach 2.4%.

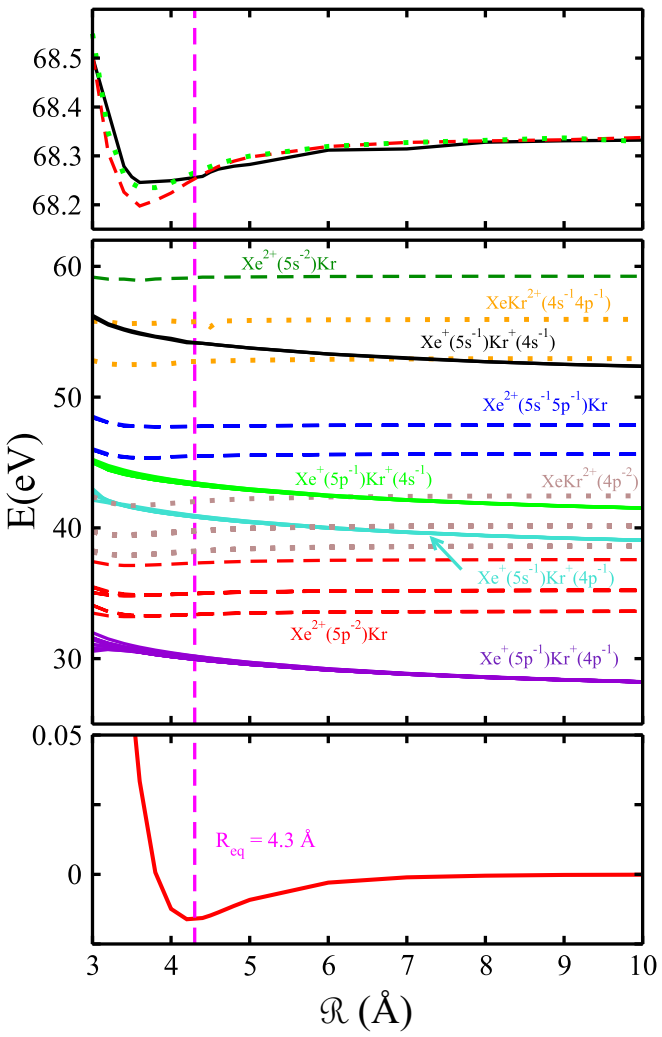

FIG. 3. Potential-energy curves (PECs) of XeKr, $Xe^+(4d^{-1})Kr$ and $(XeKr)^{2+}$ states. (bottom) The ground state of XeKr. (top) The PECs of the decaying singly ionized $Xe^+(4d^{-1})Kr$ states: $^2\Sigma$ (black solid line), $^2\Delta$ (red dashed line), $^2\Pi$ (green dotted line). (middle panel) The Auger $Xe^{2+}Kr$ (dashed lines), ICD Xe^+Kr^+ (solid lines), and ETMD $XeKr^{2+}$ (dotted lines) final states. The Auger states in order of increasing energy correspond respectively to the $Xe^{2+}(5p^{-2})Kr$, $Xe^{2+}(5p^{-1}5s^{-1})Kr$, and $Xe^{2+}(5s^{-2})Kr$ configurations. The ICD states in order of increasing energy correspond, respectively, to the $Xe^+(5p^{-1})Kr^+(4p^{-1})$, $Xe^+(5s^{-1})Kr^+(4p^{-1})$, $Xe^+(5p^{-1})Kr^+(4s^{-1})$, and $Xe^+(5s^{-1})Kr^+(4s^{-1})$ configurations. The ETMD states in order of increasing energy correspond respectively to the $XeKr^{2+}(4p^{-2})$, $XeKr^{2+}(4p^{-1}4s^{-1})$ configurations. The ground-state equilibrium distance $\mathcal{R}_{\rm eq} = 4.3$ Å of neutral XeKr is shown as a vertical dashed line.

To achieve higher ratios one should decrease the equilibrium interatomic distance in the neutral ground state. One way to do that in rare-gas dimers is to replace the neighbor with an atom which has smaller van der Waals radius. To see whether a larger ICD efficiency can be obtained we investigated the electronic decay of the $Xe^+(4d^{-1})$ state in XeKr and XeAr. The ground-state equilibrium distance of XeKr, 4.3 Å, and XeAr, 4.2 Å, is smaller than in Xe_2. There are five decaying states as shown in Figs. 3 and 4. They are bound by

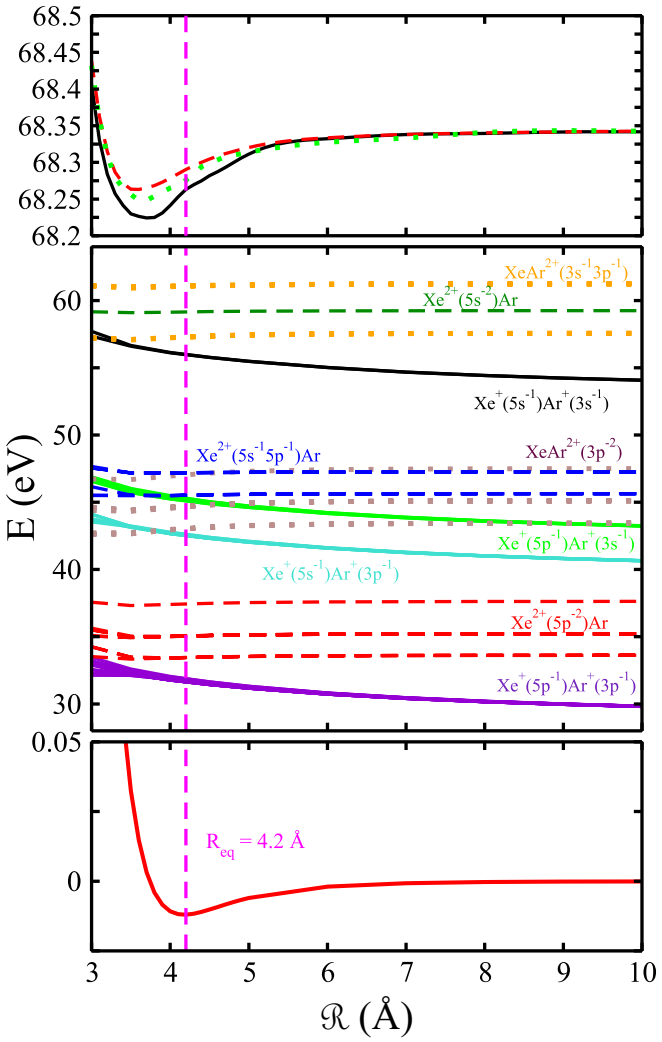

FIG. 4. Potential-energy curves (PECs) of XeAr, $Xe^{+}(4d^{-1})Ar$ and $(XeAr)^{2+}$ states. (bottom) The ground state of XeAr. (top) The PECs of the decaying singly ionized $Xe^{+}(4d^{-1})Ar$ states: $^2\Sigma$ (black solid line), $^2\Delta$ (red dashed line), $^2\Pi$ (green dotted line). (middle panel) The Auger $Xe^{2+}Ar$ (dashed lines), ICD $Xe^{+}Ar^{+}$ (solid lines), and ETMD $XeAr^{2+}$ (dotted lines) final states. The Auger states in order of increasing energy correspond respectively to the $Xe^{2+}(5p^{-2})Ar$, $Xe^{2+}(5p^{-1}5s^{-1})Ar$, and $Xe^{2+}(5s^{-2})Ar$ configurations. The ICD states in order of increasing energy correspond respectively to the $Xe^{+}(5p^{-1})Ar^{+}(3p^{-1})$, $Xe^{+}(5s^{-1})Ar^{+}(3p^{-1})$, $Xe^{+}(5p^{-1})Ar^{+}(3s^{-1})$, and $Xe^{+}(5s^{-1})Ar^{+}(3s^{-1})$ configurations. The ETMD states in order of increasing energy correspond respectively to the $XeAr^{2+}(3p^{-2})$, $XeAr^{2+}(3p^{-1}3s^{-1})$ configurations. The ground-state equilibrium distance $\mathcal{R}_{eq} = 4.2$ Å of neutral XeAr is shown as a vertical dashed line.

100—200 meV, similarly to the case of the respective PECs in Xe_2. The major differences between the homonuclear and heteronuclear dimers show up in the structure of the final states. First, due to the higher ionization potentials of Kr and Ar the principal ICD final states, $Xe^{+}(5p^{-1})Ar^{+}(3p^{-1})$ and $Xe^{+}(5p^{-1})Kr^{+}(4p^{-1})$, lie closer to the principal Auger final states, $Xe^{2+}(5p^{-2})Ar$ and $Xe^{2+}(5p^{-2})Kr$. Therefore, the principal Auger and ICD peaks will appear closer in the electron spectra of the heteronuclear clusters. Second, ETMD

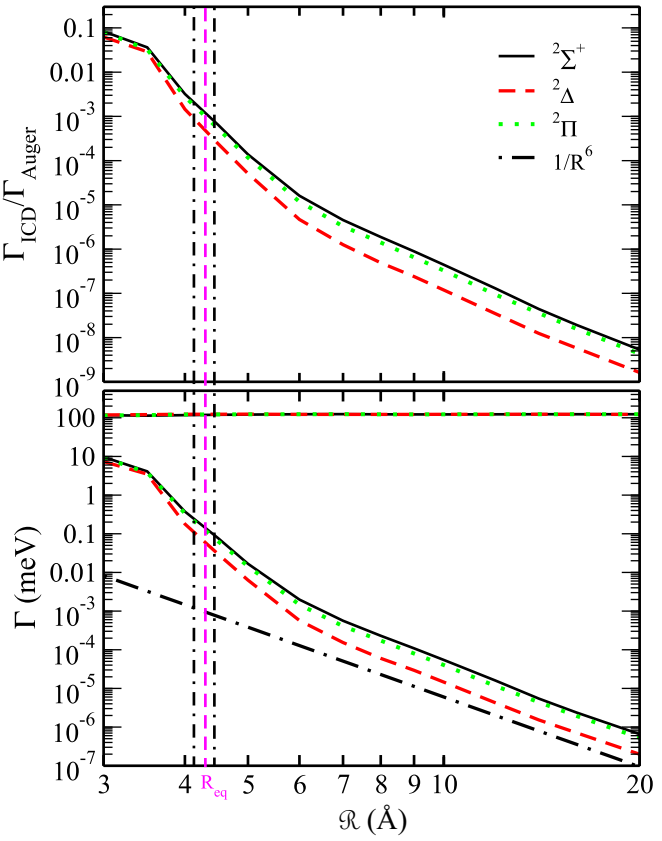

FIG. 5. (bottom) Auger (horizontal lines at 125 meV) and ICD partial decay widths of the decaying singly ionized $Xe^{+}(4d^{-1})Kr$ states. The ICD widths of the $Xe^{+}(4d^{-1})Kr$ states—$^2\Sigma$ (black solid line), $^2\Delta$ (red dashed line), $^2\Pi_g$ (green dotted line)—show the characteristic $\mathcal{R}^{-6}$ behavior of the energy-transfer processes at large distances, while they deviate from it due to the effect of orbital overlap starting at 6 Å. The plot of the $\mathcal{R}^{-6}$ function (dashed-dotted line) is included to accentuate the behavior of ICD widths at large $\mathcal{R}$. (top) ICD-to-Auger branching ratios. The ground-state equilibrium distance $\mathcal{R}_{eq}$ of the neutral XeKr is shown as a vertical dashed line. The Franck-Condon region is marked by the dashed-dotted vertical lines.

final states, $XeAr^{2+}$ and $XeKr^{2+}$, are distinguishable from the Auger ones. The probability of populating these states in the electronic decay is, like before, negligible. Indeed, we estimated the ETMD efficiency in XeAr to be less than 5% of the ICD efficiency. However, some of them might be populated in the final state's nuclear dynamics. Thus, ICD into the $Xe^{+}(5s^{-1})Kr^{+}(4p^{-1})$ and $Xe^{+}(5p^{-1})Kr^{+}(4s^{-1})$ final states will lead to the dissociative dynamics along the respective PECs and to populating of the $XeKr^{2+}(4p^{-2})$ ETMD final states through the avoided crossings at $\mathcal{R} = 6$ Å. Similar crossings between the dissociative ICD and bound ETMD final states exist also in XeAr.

The ICD and Auger partial decay widths of the $Xe^{+}(4d^{-1})Kr$ and $Xe^{+}(4d^{-1})Ar$ states and their ratios are shown in Figs. 5 and 6, respectively. Like in Xe_2 the Auger width remains virtually constant at all interatomic distances of interest and it does not vary among the different molecular terms. The ICD width increases to 11.5 meV as $\mathcal{R}$ approaches the inner turning point of the decaying state's PEC at 3.1 Å.

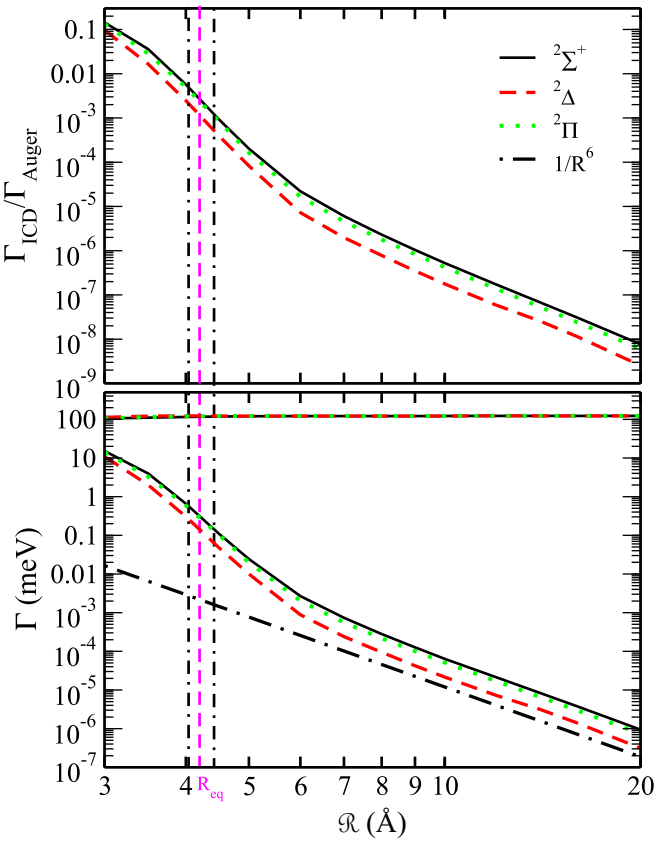

FIG. 6. (bottom) Auger (horizontal lines at 125 meV) and ICD partial decay widths of the decaying singly ionized $Xe^+(4d^{-1})Ar$ states. The ICD widths of the $Xe^+(4d^{-1})Ar$ states—$^2\Sigma$ (black solid line), $^2\Delta$ (red dashed line), $^2\Pi_g$ (green dotted line)—show the characteristic $\mathcal{R}^{-6}$ behavior of the energy-transfer processes at large distances, while they deviate from it due to the effect of orbital overlap starting at 6 Å. The plot of the $\mathcal{R}^{-6}$ function (dashed-dotted line) is included to accentuate the behavior of ICD widths at large $\mathcal{R}$. (top) ICD-to-Auger branching ratios. The ground-state equilibrium distance $\mathcal{R}_{eq}$ of the neutral XeAr is shown as a vertical dashed line. The Franck-Condon region is marked by the dashed-dotted vertical lines.

At this point it constitutes 9% of the Auger width. This high value of the ICD width reflects a strong mixing of the $Xe^{2+}(5p^{-2})Ar$ Auger and $Xe^+(5p^{-1})Ar^+(3p^{-1})$ ICD final states, which are less energetically separated than the analogous states in the two other dimers. The overall behavior of the ICD widths is similar to the one in Xe_2. They behave as $1/\mathcal{R}^6$ at larger interatomic distances, and they become enhanced at shorter distances where the orbital overlap becomes noticeable. The effect of the symmetry of the decaying state on the ICD width is more pronounced in the heteronuclear dimers. For example, the ICD of the Δ term can proceed only via Π-Π coupling between the transition moments on Xe and its neighbor, while no such restriction exists for the Σ and Π terms. As a result, the ICD width of the Δ state is four (three) times lower than the width of the Σ state in XeKr (XeAr).

The ICD partial widths at $\mathcal{R}_{eq}$ lie between 0.06 and 0.15 meV for XeKr, and 0.15 and 0.32 meV for XeAr. The largest ICD-to-Auger branching ratio in the Franck-Condon region is, therefore, 0.12% and 0.26% for XeKr and XeAr, respectively. We see that the efficiency in XeAr is, as expected, larger than in Xe_2. What is surprising is that shorter equilibrium interatomic distance in XeKr does not translate into increased ICD-to-Auger ratio. This can be explained by the fact that the ICD efficiency depends not only on the interatomic distance, but also on how easy it is to ionize the neighbor when a certain amount of energy is transferred to it. In the case of the 5p → 4d transition in Xe, approximately 57 eV of energy is released as a "virtual photon." We might take the photoionization cross section as a measure of ionization efficiency. It amounts to 1.23 Mb for Xe, 0.78 Mb for Kr, and 1.01 Mb for Ar at 57 eV photon energy [75]. Therefore, any gain in ICD efficiency in XeKr due to smaller $\mathcal{R}_{eq}$ is negated by the smaller probability of ionizing Kr compared with Xe. We can also estimate the ICD efficiency in larger mixed clusters. Such clusters have a shell structure [76] with Xe forming a core and the lighter element the outer shell, so that ICD between Xe and Ar (or Kr) occurs at the core-shell interface. We assume for simplicity that a Xe atom at the interface has six Ar (Kr) neighbors and six Xe neighbors. The largest ICD-to-Auger ratio is 2.7% in a large XeAr cluster, of which 1.5% are due to ICD with the Ar layer. The corresponding number in XeKr is 1.9%, of which 0.7% is the ratio for ICD between Xe and Kr.

TABLE I. Equilibrium distances, ICD widths, and maximum ICD-to-Auger ratios in different rare-gas dimers.

	$\mathcal{R}_{eq}$	Γ_{ICD} (meV)	$\Gamma_{ICD}/\Gamma_{Auger}$
Xe_2	4.4	0.1–0.25	0.2 %
XeKr	4.3	0.06–0.15	0.12 %
XeAr	4.2	0.15–0.32	0.26 %
Kr_2	4.0	0.06	0.09 %

Another parameter, apart from the equilibrium interatomic distance or the nature of the neighbor, which can impact the ICD-to-Auger ratio is the energy of the initial core vacancy. To see its effect we carried out the width calculations of the partial decay widths of the $3d$ vacancy in Kr_2. The maximum ICD width at the respective $\mathcal{R}_{eq} = 4.0$ Å was found to be 0.058 meV, while the Auger width was 68 meV, in good agreement with the values given in the literature [72]. The maximum ICD-to-Auger ratio in Kr_2 is only 0.085%, considerably less than in the XeRG dimers, even though the decay occurs at much shorter interatomic distances. Its smallness compared with the results in pure and mixed Xe dimers can be explained by inefficient ionization of a neighbor at high values of transferred energy.

Since the lifetimes of the core vacancies are of order of a few femtoseconds, the electronic decay occurs in the Franck-Condon region of the respective dimer. Therefore, to be able to compare the efficiency of the different decay mechanisms in different dimers more easily, we collated the ICD-to-Auger ratios at the respective ground-state equilibrium distances $\mathcal{R}_{eq}$ in Table I.

IV. CONCLUSIONS

In this work, we studied electronic decay of core-hole vacancies in rare-gas dimers. Our goal was to determine the

efficiency of the nonlocal core-level ICD process as compared with the local Auger decay. We computed the ICD and Auger partial decay widths and their ratios for $Xe^+(4d^{-1})$-R (R = Xe, Kr, Ar) and $Kr^+(3d^{-1})$Kr states. In all the dimers the Auger decay remains a local process, which populates two-hole states at the core-vacancy site and whose width is independent of the distances between the excited atom and its neighbor. The ICD width grows strongly with decreasing distance, decreases with the increasing energy of the initial core-hole state, and varies within a factor of two for different neighbors.

If one considers the absolute value of the ICD-to-Auger ratio in these dimers one notes that ICD contribution to the electronic decay is small. The largest value obtained in XeAr is 0.26%. It is improbable that this ratio may be increased by the decay occurring at shorter interatomic distances, since no nuclear dynamics can take place in the decaying state during its very short lifetime. The role of ICD will be greater in larger clusters, since ICD width grows with the number of neighbors around the core-hole site. We found that the ratio in larger Xe cluster can reach 2.4%, while in mixed XeAr clusters this ratio reaches 2.7%. Recent experiments in larger Ar clusters found the core ICD-to-Auger branching ratio of 0.8%, which is in line with the results obtained in this work [36]. Therefore, the rare-gas clusters can be used to study core-level ICD and its competition with Auger decay. However, the impact of this process on charge redistribution in such clusters under normal conditions, while not completely negligible, is moderate at best.

In what systems and under what circumstances will core-level ICD be important? Our results indicate that the distance between the monomers is the most important parameter which defines ICD efficiency. Could one bring $Xe^+(4d^{-1})$ and Ar atoms in the respective dimer to the inner classical turning point of the decaying PEC (3.1 Å), one would reach an ICD-to-Auger branching ratio up to 9%. In bigger clusters with multiple neighbors, that would result in comparable rates of ICD and Auger decay. Since the decay will invariably take place in the Franck-Condon region, one should select systems with shorter distances between the monomers in the ground state. One possibility will be to subject rare gases to high pressure; the Xe -Xe distance becomes as short as 3.3 Å at 100 GPa [77]. The hydrogen-bonded or microsolvated clusters, e.g., those which comprise a metal cation (such as Li^+ or Mg^{2+}) and molecular ligands [11,78], offer an alternative class of weakly bound systems for studying the core-level ICD process. The characteristic equilibrium distances between the monomers in such systems are between 2 and 3 Å, and ICD-to-Auger ratios up to 10% can be observed [22]. Also, since ICD is efficient for smaller values of transferred energy, its share in the total decay width will be large either in the case of shallow core vacancies or Coster-Kronig transitions. Thus, while of limited importance in rare-gas atoms, core-level ICD might efficiently drive charge redistribution during Auger cascades in microsolvated clusters, liquid solutions, or at metal-containing active sites of biomolecules.

ACKNOWLEDGMENTS

The authors would like to thank L. S. Cederbaum and N. V. Kryzhevoi for reading and commenting on the paper, and A. Ghosh and E. V. Gromov for their help with the computations. Financial support by the European Research Council (ERC) (Advanced Investigator Grant No. 692657), the Science Challenge Project Grant No. TZ2018005, and the National Key R&D Program of China (Grant No. 2017YEFA0403202) is gratefully acknowledged. P.K. acknowledges financial support by the Czech Science Foundation (Project GAČR No. 17-10866S).

[1] A. Rudenko, L. Inhester, K. Hanasaki, X. Li, S. J. Robatjazi, B. Erk, R. Boll, K. Toyota, Y. Hao, O. Vendrell, C. Bomme, E. Savelyev, B. Rudek, L. Foucar, S. H. Southworth, C. S. Lehmann, B. Kraessig, T. Marchenko, M. Simon, K. Ueda *et al.*, Nature (London) **546**, 129 (2017).

[2] B. Erk, R. Boll, S. Trippel, D. Anielski, L. Foucar, B. Rudek, S. W. Epp, R. Coffee, S. Carron, S. Schorb, K. R. Ferguson, M. Swiggers, J. D. Bozek, M. Simon, T. Marchenko, J. Küpper, I. Schlichting, J. Ullrich, C. Bostedt, D. Rolles, and A. Rudenko, Science **345**, 288 (2014).

[3] K. Motomura, E. Kukk, H. Fukuzawa, S.-i. Wada, K. Nagaya, S. Ohmura, S. Mondal, T. Tachibana, Y. Ito, R. Koga, T. Sakai, K. Matsunami, A. Rudenko, C. Nicolas, X.-J. Liu, C. Miron, Y. Zhang, Y. Jiang, J. Chen, M. Anand *et al.*, J. Phys. Chem. Lett. **6**, 2944 (2015).

[4] K. Nagaya, K. Motomura, E. Kukk, H. Fukuzawa, S. Wada, T. Tachibana, Y. Ito, S. Mondal, T. Sakai, K. Matsunami, R. Koga, S. Ohmura, Y. Takahashi, M. Kanno, A. Rudenko, C. Nicolas, X.-J. Liu, Y. Zhang, J. Chen, M. Anand *et al.*, Phys. Rev. X **6**, 021035 (2016).

[5] T. Takanashi, K. Nakamura, E. Kukk, K. Motomura, H. Fukuzawa, K. Nagaya, S.-i. Wada, Y. Kumagai, D. Iablonskyi, Y. Ito, Y. Sakakibara, D. You, T. Nishiyama, K. Asa, Y. Sato, T. Umemoto, K. Kariyazono, K. Ochiai, M. Kanno, K. Yamazaki *et al.*, Phys. Chem. Chem. Phys. **19**, 19707 (2017).

[6] H. Fukuzawa, T. Takanashi, E. Kukk, K. Motomura, S. Wada, K. Nagaya, Y. Ito, T. Nishiyama, C. Nicolas, Y. Kumagai, D. Iablonskyi, S. Mondal, T. Tachibana, D. You, S. Yamada, Y. Sakakibara, K. Asa, Y. Sato, T. Sakai, K. Matsunami *et al.*, Nat. Commun. **10**, 2186 (2019).

[7] S. P. Hau-Riege, R. A. London, H. N. Chapman, A. Szoke, and N. Timneanu, Phys. Rev. Lett. **98**, 198302 (2007).

[8] S. P. Hau-Riege, S. Boutet, A. Barty, S. Bajt, M. J. Bogan, M. Frank, J. Andreasson, B. Iwan, M. M. Seibert, J. Hajdu, A. Sakdinawat, J. Schulz, R. Treusch, and H. N. Chapman, Phys. Rev. Lett. **104**, 064801 (2010).

[9] M. Hoener, C. Bostedt, H. Thomas, L. Landt, E. Eremina, H. Wabnitz, T. Laarmann, R. Treusch, A. R. B. de Castro, and T. Möller, J. Phys. B: At., Mol. Opt. Phys. **41**, 181001 (2008).

[10] B. Ziaja, H. N. Chapman, R. Santra, T. Laarmann, E. Weckert, C. Bostedt, and T. Möller, Phys. Rev. A **84**, 033201 (2011).

[11] V. Stumpf, K. Gokhberg, and L. S. Cederbaum, Nat. Chem. **8**, 237 (2016).

[12] V. Stumpf, S. Scheit, P. Kolorenč, and K. Gokhberg, Chem. Phys. **482**, 192 (2017).

[13] D. You, H. Fukuzawa, Y. Sakakibara, T. Takanashi, Y. Ito, G. G. Maliyar, K. Motomura, K. Nagaya, T. Nishiyama, K. Asa, Y. Sato, N. Saito, M. Oura, M. Schöffler, G. Kastirke, U. Hergenhahn, V. Stumpf, K. Gokhberg, A. I. Kuleff, L. S. Cederbaum *et al.*, Nat. Commun. **8**, 14277 (2017).

[14] P. H. Citrin, Phys. Rev. Lett. **31**, 1164 (1973).

[15] J. A. D. Matthew and Y. Komninos, Surf. Sci. **53**, 716 (1975).

[16] L. S. Cederbaum, J. Zobeley, and F. Tarantelli, Phys. Rev. Lett. **79**, 4778 (1997).

[17] S. Barth, S. Joshi, S. Marburger, V. Ulrich, A. Lindblad, G. Öhrwall, O. Björneholm, and U. Hergenhahn, J. Chem. Phys. **122**, 241102 (2005).

[18] K. Gokhberg, V. Averbukh, and L. S. Cederbaum, J. Chem. Phys. **124**, 144315 (2006).

[19] T. Aoto, K. Ito, Y. Hikosaka, E. Shigemasa, F. Penent, and P. Lablanquie, Phys. Rev. Lett. **97**, 243401 (2006).

[20] A. Knie, A. Hans, M. Förstel, U. Hergenhahn, P. Schmidt, P. Reiß, C. Ozga, B. Kambs, F. Trinter, J. Voigtsberger, D. Metz, T. Jahnke, R. Dörner, A. I. Kuleff, L. S. Cederbaum, P. V. Demekhin, and A. Ehresmann, New J. Phys. **16**, 102002 (2014).

[21] W. Pokapanich, H. Bergersen, I. L. Bradeanu, R. Marinho, A. Lindblad, S. Legendre, A. Rosso, S. Svensson, O. Björneholm, M. Tchaplyguine, G. Öhrwall, N. V. Kryzhevoi, and L. S. Cederbaum, J. Am. Chem. Soc. **131**, 7264 (2009).

[22] W. Pokapanich, N. V. Kryzhevoi, N. Ottosson, S. Svensson, L. S. Cederbaum, G. Öhrwall, and O. Björneholm, J. Am. Chem. Soc. **133**, 13430 (2011).

[23] P. H. Citrin, P. M. Eisenberger, W. C. Marra, T. Åberg, J. Utriainen, and E. Källne, Phys. Rev. B **10**, 1762 (1974).

[24] J. A. D. Matthew and M. G. Devey, J. Phys. C: Solid State Phys. **7**, L335 (1974).

[25] C. Buth, R. Santra, and L. S. Cederbaum, J. Chem. Phys. **119**, 10575 (2003).

[26] G. Öhrwall, R. F. Fink, M. Tchaplyguine, L. Ojamäe, M. Lundwall, R. R. T. Marinho, A. Naves de Brito, S. L. Sorensen, M. Gisselbrecht, R. Feifel, T. Rander, A. Lindblad, J. Schulz, L. J. Sæthre, N. Mårtensson, S. Svensson, and O. Björneholm, J. Chem. Phys. **123**, 054310 (2005).

[27] P. Slavíček, B. Winter, L. S. Cederbaum, and N. V. Kryzhevoi, J. Am. Chem. Soc. **136**, 18170 (2014).

[28] P. Slavíček, N. V. Kryzhevoi, E. F. Aziz, and B. Winter, J. Phys. Chem. Lett. **7**, 234 (2016).

[29] J. L. Hemmerich, R. Bennett, and S. Y. Buhmann, Nat. Commun. **9**, 2934 (2018).

[30] V. Averbukh, I. B. Müller, and L. S. Cederbaum, Phys. Rev. Lett. **93**, 263002 (2004).

[31] K. Gokhberg, S. Kopelke, N. V. Kryzhevoi, P. Kolorenč, and L. S. Cederbaum, Phys. Rev. A **81**, 013417 (2010).

[32] J. S. Rao, T. C. Dinadayalane, J. Leszczynski, and G. N. Sastry, J. Phys. Chem. A **112**, 12944 (2008).

[33] E. Rühl, Int. J. Mass Spectrom. **229**, 117 (2003).

[34] T. Jahnke, J. Phys. B: At., Mol. Opt. Phys. **48**, 082001 (2015).

[35] A. Hans, C. Ozga, P. Schmidt, G. Hartmann, A. Nehls, P. Wenzel, C. Richter, C. Lant, X. Holzapfel, J. H. Viehmann, U. Hergenhahn, A. Ehresmann, and A. Knie, Rev. Sci. Instrum. **90**, 093104 (2019).

[36] A. Hans, C. Küstner-Wetekam, P. Schmidt, C. Ozga, X. Holzapfel, H. Otto, C. Zindel, C. Richter, L. S. Cederbaum, A. Ehresmann, U. Hergenhahn, N. V. Kryzhevoi, and A. Knie, Phys. Rev. Res. **2**, 012022(R) (2020).

[37] A. E. Kramida, Y. Ralchenko, J. Reader, and NIST ASD TEAM, *NIST Atomic Spectra Database* (version 5.6.1); http://physics.nist.gov/asd (National Institute of Standards and Technology, Gaithersburg, 2018).

[38] J. Schirmer, L. S. Cederbaum, and O. Walter, Phys. Rev. A **28**, 1237 (1983).

[39] J. Schirmer and A. Barth, Z. Phys. A: At. Nucl. (1975) **317**, 267 (1984).

[40] P. H. P. Harbach, M. Wormit, and A. Dreuw, J. Chem. Phys. **141**, 064113 (2014).

[41] K. A. Peterson and T. H. Dunning Jr., J. Chem. Phys. **117**, 10548 (2002).

[42] K. A. Peterson and K. E. Yousaf, J. Chem. Phys. **133**, 174116 (2010).

[43] K. A. Peterson, D. Figgen, E. Goll, H. Stoll, and M. Dolg, J. Chem. Phys. **119**, 11099 (2003).

[44] H. Meyer and S. Pal, J. Chem. Phys. **91**, 6195 (1989).

[45] R. A. Aziz and H. H. Chen, J. Chem. Phys. **67**, 5719 (1977).

[46] P. Slavíček, R. Kalus, P. Paška, I. Odvárková, P. Hobza, and A. Malijevský, J. Chem. Phys. **119**, 2102 (2003).

[47] H.-J. Werner, P. J. Knowles, G. Knizia, F. R. Manby, M. Schütz, P. Celani, T. Korona, R. Lindh, A. Mitrushenkov, G. Rauhut, K. R. Shamasundar, T. B. Adler, R. D. Amos, A. Bernhardsson, A. Berning, D. L. Cooper, M. J. O. Deegan, A. J. Dobbyn, F. Eckert, E. Goll, C. Hampel, A. Hesselmann, G. Hetzer, T. Hrenar, G. Jansen, C. Köppl, Y. Liu, A. W. Lloyd, R. A. Mata, A. J. May, S. J. McNicholas, W. Meyer, M. E. Mura, A. Nicklass, D. P. O'Neill, P. Palmieri, D. Peng, K. Pflüger, R. Pitzer, M. Reiher, T. Shiozaki, H. Stoll, A. J. Stone, R. Tarroni, T. Thorsteinsson, and M. Wang, Molpro, version 2010.1, A Package of *Ab Initio* Programs (2012), https://www.molpro.net.

[48] M. H. Beck, A. Jäckle, G. A. Worth, and H.-D. Meyer, Phys. Rep. **324**, 1 (2000).

[49] V. Averbukh and L. S. Cederbaum, J. Chem. Phys. **123**, 204107 (2005).

[50] U. Fano, Phys. Rev. **124**, 1866 (1961).

[51] H. Feshbach, Ann. Phys. (NY) **19**, 287 (1962).

[52] F. Mertins and J. Schirmer, Phys. Rev. A **53**, 2140 (1996).

[53] P. Kolorenč and N. Sisourat, J. Chem. Phys. **143**, 224310 (2015).

[54] W. P. Reinhardt, Comput. Phys. Commun. **17**, 1 (1979).

[55] A. U. Hazi, J. Phys. B: At. Mol. Phys. **11**, L259 (1978).

[56] F. Müller-Plathe and G. H. F. Diercksen, Phys. Rev. A **40**, 696 (1989).

[57] G. Karlström, R. Lindh, P. A. k. Malmqvist, B. O. Roos, U. Ryde, V. Veryazov, P. O. Widmark, M. Cossi, B. Schimmelpfennig, and P. Neograd, Comput. Mater. Sci. **28**, 222 (2003).

[58] K. Kaufmann, W. Baumeister, and M. Jungen, J. Phys. B: At., Mol. Opt. Phys. **22**, 2223 (1989).

[59] See Supplemental Material at http://link.aps.org/supplemental/10.1103/PhysRevA.101.033402 for the numerical values of the KBJ exponents.

[60] M. Lundwall, R. F. Fink, M. Tchaplyguine, A. Lindblad, G. Öhrwall, H. Bergersen, S. Peredkov, T. Rander, S. Svensson, and O. Björneholm, J. Phys. B: At., Mol. Opt. Phys. **39**, 5225 (2006).

[61] J. Zobeley, R. Santra, and L. S. Cederbaum, J. Chem. Phys. **115**, 5076 (2001).
[62] S. Scheit, V. Averbukh, H.-D. Meyer, J. Zobeley, and L. S. Cederbaum, J. Chem. Phys. **124**, 154305 (2006).
[63] M. Förstel, M. Mucke, T. Arion, A. M. Bradshaw, and U. Hergenhahn, Phys. Rev. Lett. **106**, 033402 (2011).
[64] K. Sakai, S. Stoychev, T. Ouchi, I. Higuchi, M. Schöffler, T. Mazza, H. Fukuzawa, K. Nagaya, M. Yao, Y. Tamenori, A. I. Kuleff, N. Saito, and K. Ueda, Phys. Rev. Lett. **106**, 033401 (2011).
[65] A. C. LaForge, V. Stumpf, K. Gokhberg, J. von Vangerow, F. Stienkemeier, N. V. Kryzhevoi, P. O'Keeffe, A. Ciavardini, S. R. Krishnan, M. Coreno, K. C. Prince, R. Richter, R. Moshammer, T. Pfeifer, L. S. Cederbaum, and M. Mudrich, Phys. Rev. Lett. **116**, 203001 (2016).
[66] V. Averbukh and P. Kolorenč, Phys. Rev. Lett. **103**, 183001 (2009).
[67] N. Saito, Y. Morishita, I. Suzuki, S. Stoychev, A. Kuleff, L. Cederbaum, X.-J. Liu, H. Fukuzawa, G. Prümper, and K. Ueda, Chem. Phys. Lett. **441**, 16 (2007).
[68] A. Hans, V. Stumpf, X. Holzapfel, F. Wiegandt, P. Schmidt, C. Ozga, P. Reiß, L. B. Ltaief, C. Küstner-Wetekam, T. Jahnke, A. Ehresmann, P. V. Demekhin, K. Gokhberg, and A. Knie, New J. Phys. **20**, 012001 (2018).
[69] E. Fasshauer, M. Pernpointner, and K. Gokhberg, J. Chem. Phys. **138**, 014305 (2013).
[70] A. Ausmees, A. Hahlin, S. L. Sorensen, S. Sundin, I. Hjelte, O. Björneholm, and S. Svensson, J. Phys. B: At., Mol. Opt. Phys. **32**, L197 (1999).
[71] A. Mäntykenttä, Phys. Rev. A **47**, 3961 (1993).
[72] E. Fasshauer, P. Kolorenč, and M. Pernpointner, J. Chem. Phys. **142**, 144106 (2015).
[73] R. Santra and L. S. Cederbaum, Phys. Rep. **368**, 1 (2002).
[74] T. Förster, Ann. Phys. (Berlin, Ger.) **437**, 55 (1948).
[75] J. Samson and W. Stolte, J. Electron Spectrosc. Relat. Phenom. **123**, 265 (2002).
[76] M. Lundwall, W. Pokapanich, H. Bergersen, A. Lindblad, T. Rander, G. Öhrwall, M. Tchaplyguine, S. Barth, U. Hergenhahn, S. Svensson, and O. Björneholm, J. Chem. Phys. **126**, 214706 (2007).
[77] K. A. Goettel, J. H. Eggert, I. F. Silvera, and W. C. Moss, Phys. Rev. Lett. **62**, 665 (1989).
[78] I. B. Müller and L. S. Cederbaum, J. Chem. Phys. **122**, 094305 (2005).